Journal of Nanotechnology & Advanced Materials
An International Journal

http://dx.doi.org/10.18576/jnam/120101

A Study of Ti Incorporation in ZnO Nanoflakes Synthesized by Citrate Route Method

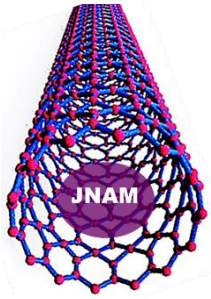

H. Ibrahim[1], M. Abdel-Rahman[1], Hani Khallaf[1] and Emad A. Badawi[1,]*

[1] Department of Physics, Faculty of Science, Minia University, Minia City, 61519, Egypt.

Received: 05 Oct. 2024, Revised: 07 Oct. 2024, Accepted: 13 Oct. 2024.
Published online: 1 Nov 2024.

Abstract: In this paper, Ti-doped ZnO nanostructures are synthesized using citric acid sol-gel (citrate route) method. Synthesized nanostructures are calcined at two different temperatures; 400 and 600 °C. A comprehensive study of the effect of Ti incorporation on the crystal structure, nanostructures size, shape, and elemental composition, as well as the optical properties of the doped ZnO nanostructures is reported. Mixed phases of hexagonal ZnO and cubic $ZnTiO_3$ are detected at high Ti concentrations (≥12%) and calcination temperatures of 600 °C. This is further confirmed by optical studies where absorbance as well as diffuse reflectance edges characteristic of $ZnTiO_3$ are detected. XRD studies confirm the successful doping and provide a clear indication that Ti is replacing the Zn atoms substitutionally. Doped ZnO morphology changed from nanoflakes to nanostructures with porous nature as Ti content increases. EDX analysis shows the Ti content to increase as the Ti/Zn molar ratio increases in the synthesized samples. The optical bandgap is found to be sensitive to the Ti content and can be tuned by varying the Ti concentration.

Keywords: Ti-doped ZnO nanostructures, ZnO – $ZnTiO_3$ nanocomposites, XRD, SEM, EDX.

1. Introduction

Zinc oxide (ZnO) is a wide bandgap semiconductor material (Eg ~ 3.37 eV), with a high transmission in the visible region, high electron mobility as well as excellent photoluminescence properties [1, 2]. ZnO doped with transition metals has the potential to be a highly functional material with coexisting magnetic, semiconducting, electromechanical, and optical properties [3]. Meanwhile, ZnO nanomaterials coupled with other metal oxide semiconductors facilitate enhanced photocatalytic activity [4].

Titanium doping of ZnO oxide has recently drawn a lot of attention due to the fact that, unlike group III elements (such as B, Al, Ga, and In), Ti-doping can provide two loosely-bound electrons per atom which, in turn, enhances the conductivity and photoresponse of the ZnO host [5]. It has been previously reported that, in comparison with pure ZnO, Ti-doped ZnO has enhanced green emission [6, 7]. Furthermore, Ti-doping of ZnO has been heavily investigated because of ZnO wide applications in gas sensors, light-emitting diodes, solar cells, UV lasers, UV photodetectors, field-effect transistors, piezoelectric transducers, antibacterial and UV protection, as well as many other biomedical and optoelectronic applications. Incorporation of Ti in ZnO nanostructures may also result in the formation of mixed oxide nanocomposites of ZnO-TiO_2. In fact, Ti incorporation into the ZnO structure, both as a dopant or in the form of a mixed oxide, is not yet fully understood. In addition, upon calcination of ZnO-TiO_2 composites at 500, 600 and 700 °C, different products are synthesized [7, 8]:

$$ZnO + TiO_2 \rightarrow ZnTiO_3 \quad (1)$$

$$2ZnO + TiO_2 \rightarrow Zn_2TiO_4 \quad (2)$$

$$2ZnO + 3TiO_2 \rightarrow Zn_2Ti_3O_8 \quad (3)$$

Zinc titanate ($ZnTiO_3$), for example, has superior electrical properties that are useful for applications towards microwave dielectrics.

Interest in ZnO-TiO_2 compounds arises from the fact that they have characteristics common to both individual oxides [2, 9-13]. Moreover, ZnO as well as TiO_2 nanostructures are known to have enhanced performance over the bulk material with numerous applications in photocatalysis, biomedicine, optical detection and bioimaging [14-21]. ZnO-TiO_2 nanocomposite formation has been previously studied by many research groups [22-40] where improvement in Sun Protection Factor (SPF) [23], higher transparency in the visible region [24], and greater photocatalytic activity [25-29] have been reported. Further applications in dye-sensitized solar cells, ink and herbicide degradation, gas sensors, and photocatalysis for water splitting have been extensively investigated [30-40].

In the meantime, various methods have been employed to synthesize ZnO-TiO_2 nanocomposites such as chemical vapor deposition, sol-gel, combustion, ultrasonic spray pyrolysis, hydrothermal, coprecipitation, electrospinning, thermal decomposition of salts, etc. [13, 29, 41-47]. The synthesis mechanism, however, has a deep impact on the structure, physical and chemical properties of the nanocomposites [24, 48].

Sol-gel, which is the synthesis method employed in this

*Corresponding author e-mail: emad.badawi@mu.edu.eg

work, is considered as one of the most popular methods to grow metal oxide nanostructures because of its simplicity, reliability, reproducibility, and cost effectiveness [49-53]. In the citric acid sol-gel (citrate route) method, citric acid which is an effective chelating agent is mixed with an aqueous metal salt and the prepared solution is heated up to form a viscous solution or Gel. As the "metal-citrate" gel is heated, the organic component burns at ~ 250 – 300 °C. Milling and then annealing the resulting powder produce the metal oxide nanostructures. During the sol-gel synthesis process, citric acid acts as a chelating agent for metal ions as well as an organic fuel during the calcination process.

In the present work, ZnO nanoflakes and Ti-doped ZnO nanostructures with different titanium content were synthesized using citrate route method. The synthesized nanostructures are calcined at two different temperatures: 400 and 600 °C. The Ti-doping effect on the crystal structure, nanostructures size, shape, and elemental composition, as well as the optical properties of the doped ZnO nanostructures are studied using X-ray diffraction (XRD), scanning electron microscopy (SEM) and energy dispersive X-ray (EDX) analysis, and UV-V is spectroscopy, respectively. The lattice parameters, crystallite size, micro-strain, Zn–O bond length, and d-spacing of the obtained samples are calculated using Williamson-Hall [54] and Rietveld-refinement method (MAUD program) [55]. The crystallite plot of undoped as well as Ti-doped ZnO nanostructures synthesized at different Ti content is obtained using the anisotropic size-strain model (Popa rules model) [56].

2. Experimental Details

2.1 Chemicals and Synthesis

Chemical reagents used are of analytical grade (purchased from Techno PharmChem) and were used as received without additional purification. Zinc acetate dehydrates; Zn $(AC)_2.2H_2O$ and citric acid (H_3Cit or $C_6H_8O_7$) with molar ratio 1:2 is dissolved in 25 ml deionized water, separately. The citric acid solution is kept on a magnetic stirrer at room temperature and the zinc acetate dehydrates solution was added dropwise, then the reaction mixture is maintained at room temperature for about an hour [57]. For Ti-doping, a specific amount of titanium isopropoxide is added to the mixture. After 1 h, the solution is heated to 85 °C, then to 120 °C, until it turns more and more viscous and finally becomes a xerogel, and then heated again for 1 h at 250 °C for complete drying. The obtained precursor is grounded into a powder then calcined at 400 °C for 1 h then cooled down until room temperature is reached. Doping with titanium content ranging from 2 % to 20 % is investigated.

2.2 Characterization

X-ray Diffraction (XRD)

XRD measurements were carried out using JEOL X-ray unit (Model JSDX-60PA) equipped with a Cukα-radiation ($\lambda = 0.154184$nm). X-ray source was operated at 40kV and 35mA. Samples were scanned from 30° to 100° with continuous slow scanning rate (1° min^{-1}) and a small (1 sec) time constant.

Scanning Electron Microscopy (SEM) and Energy Dispersive X-ray (EDX) Analysis

Nanostructure size and elemental composition of the synthesized samples were studied using JEOL Scanning Electron Microscope (Model JSM – IT 200) with an operating voltage of 25 kV.

Ultraviolet-Visible (UV-Vis) spectroscopy

The optical characterization was carried out by measuring the absorbance as well as the diffuse reflectance spectroscopy in UV-Vis range, which result from the electronic transitions of a solid structure when irradiated with ultraviolet or visible light. With the help of the resulting absorption/ diffuse reflectance spectra, the magnitude of the bandgap is calculated [58]. Spectra were obtained using JASCO V-670 UV-Vis-NIR spectrophotometer in the range from 200 nm to 800 nm, at 100 nm/min scanning speed. Barium sulfate ($BaSO_4$) was used as the reference material.

3. Results and Discussion

3.1 X-ray Diffraction

The powder XRD pattern (Fig. 1a) of the prepared samples calcined at 400 °C for 1 h with different Ti concentrations shows pure hexagonal wurtzite ZnO structure with a main (101) reflection and eight other reflections characteristic of the (100), (002), (102), (110), (103), (200), (112), and (201) planes (JCPDS card No. 80-0075). However, the XRD pattern of the sample with 14% and 20% Ti concentration calcined at 600 °C (Fig. 1b) shows mixed ZnO and ZnTiO3 phases, with new reflections characteristic of the (220), (311), (400), (422), and (440) planes of the ZnTiO3 cubic phase (JCPDS card No. 39-0190). The content of the ZnO and ZnTiO3 phases in each XRD pattern are determined using the following equations [6]:

$$ZnO\ (\%) = \frac{I_{Zn}(101)}{I_{ZT}(311)+I_{Zn}(101)} \times 100 \quad (4)$$

$$ZnTiO_3\ (\%) = \frac{I_{ZT}(311)}{I_{ZT}(311)+I_{Zn}(101)} \times 100 \quad (5)$$

where $I_{Zn}(101)$ and $I_{ZT}(311)$ denote the relative integral intensities of (101) and (311) for the ZnO and $ZnTiO_3$ phases, respectively.

We have observed that at low Ti concentration, only Ti-doped ZnO nanostructures are formed while at high concentrations (≥12%) mixed oxide nanocomposites of ZnO – $ZnTiO_3$ are formed. Table 1 indicates that the content of zinc titanate (~ 42%) is independent of the Ti concentration, which means that, at high Ti content, part of the Ti^{4+} ions are still replacing Zn^{2+} ions substitutionally in

the ZnO host and Ti-doping coexists with mixed oxide formation of ZnO – $ZnTiO_3$. Formation of mixed zinc oxide – zinc titanate composites at high Ti content and high calcination temperature has been previously reported [6, 7].

Table 1: ZnO and $ZnTiO_3$ phases content of samples calcined at 600 °C.

Ti – content	I_{311}	I_{101}	ZnO%	$ZnTiO_3$%
14 %	570	790	58.08	41.91
20 %	560	775	58.05	41.94

ZnO – TiO_2 as well as other Zn – Ti mixed oxide formation at high Ti content has also been reported [8, 59]. $ZnTiO_3$ cubic and hexagonal phases have also been detected at high calcination temperatures [60, 61]. The proposed mechanism for $ZnTiO_3$ formation at high calcination temperatures is the following [61]:

$$3ZnTi(OH)_6 \xrightarrow{<400\ ^\circ C} Zn_2Ti_3O_8\ (amorphous) + ZnO + 9H_2O \quad (6)$$

$$Zn_2Ti_3O_8\ (amorphous) + ZnO \xrightarrow{400\ ^\circ C-500^\circ C} Zn_2Ti_3O_8\ (cubic) + ZnO \quad (7)$$

$$Zn_2Ti_3O_8\ (cubic) + ZnO \xrightarrow{600\ ^\circ C-700^\circ C} 3ZnTiO_3\ (cubic) \quad (8)$$

$$3ZnTiO_3\ (cubic) \xrightarrow{700\ ^\circ C-900^\circ C} 2ZnTiO_3\ (cubic) + ZnTiO_3\ (\text{hexagonal}) \quad (9)$$

It is worth noting that the observed decrease in the peak intensity of the doped samples is attributed to a decrease in the crystallinity of the ZnO nanostructures with Ti-doping, especially at high Ti content.

The micro-strain (ε) of the obtained samples is calculated using Williamson–Hall method [54]:

$$B\ cos\theta = K\ \lambda/D_c + 2\varepsilon\ sin\theta \quad (10)$$

where D_c is the average crystallite size, ε is the strain introduced inside the sample, θ is the Bragg angle, λ is the wavelength, K is a constant (= 0.89), and B is the full width at half maximum (FWHM).

As shown in Fig. 2a, the crystallite size decreases with increasing Ti content in the ZnO host. Apparently, the presence of Ti^{4+} ions decrease the number of reactive Zn^{2+} ions which, in turn, results in a slow nucleation process due to the lack of zinc citrate complex formation. This will result in a smaller crystallite size. That is why the crystallite size decreases (from 44.3 nm to 17.28 nm) as the Ti content increases (from 0 % to 20 %). It is worth noting that a polymeric zinc citrate complex, $[Zn(H_2Cit)(H_2O)]_n$, is usually formed at low pH [62]:

$$Zn^{2+} + H_3Cit + H_2O \rightleftharpoons [Zn(H_2Cit)(H_2O)]_n \quad (11)$$

Thermal decomposition of the zinc citrate complex leads to the formation of zinc oxide [63]. The lack of zinc citrate complex will also have a negative impact on the crystallinity of the Ti-doped ZnO samples as indicated by the decrease in the XRD peak intensities observed in Fig. 1a.

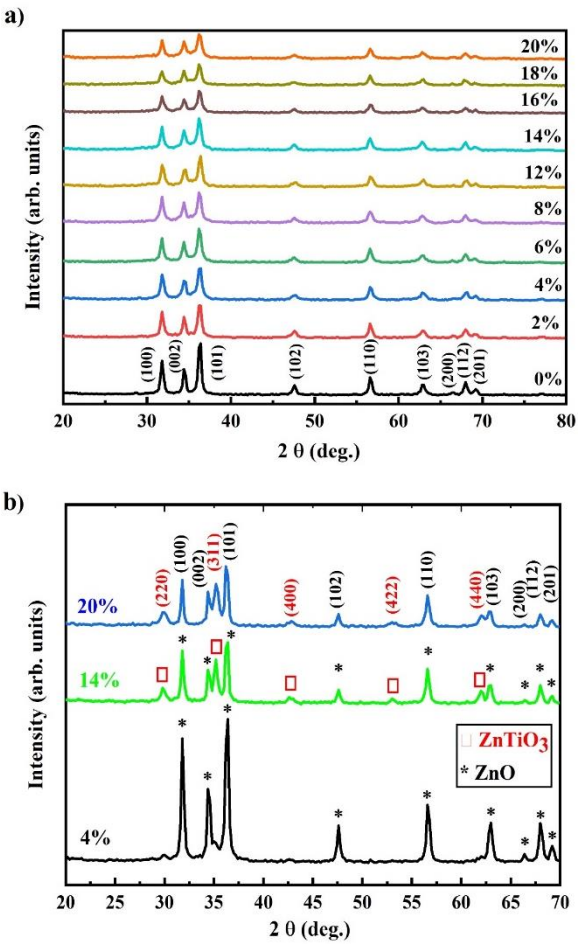

Fig. 1: XRD patterns of Ti-doped ZnO nanostructures synthesized at different Ti content: (a) calcined at 400°C; (b) calcined at 600°C.

Interestingly, lattice micro-strain is observed to vary in an opposite manner to that of the crystallite size (Fig. 2a). This can be explained when a decrease in crystallite size typically results in an increase in grain boundary regions. These regions are highly defective in nature. As a result, many defects/dislocations are introduced, and the micro-strain increases with increasing Ti content in the ZnO host.

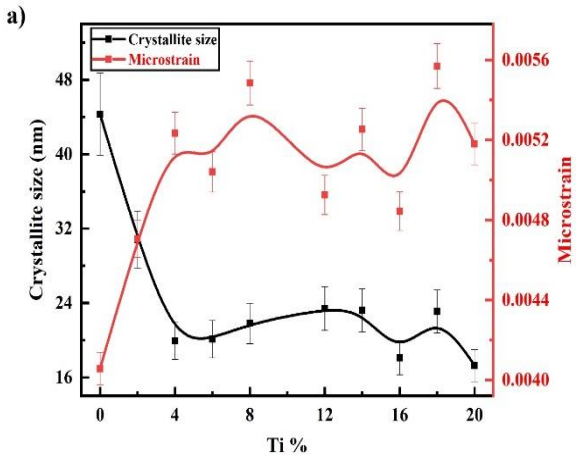

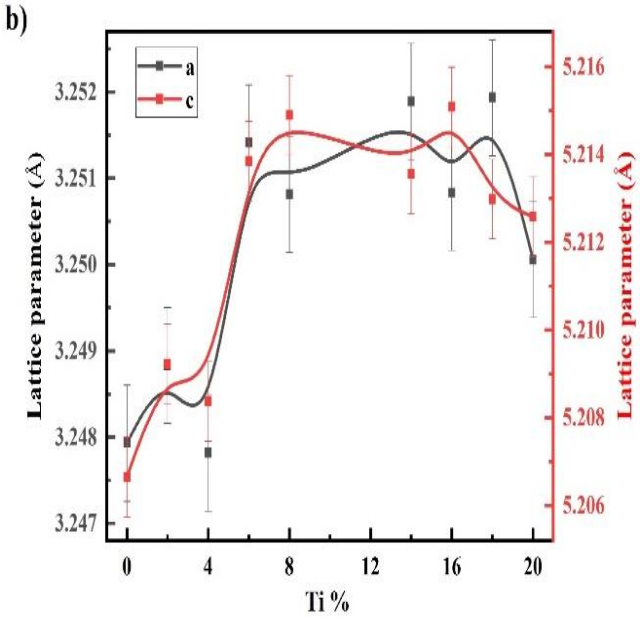

Fig. 2: a) Crystallite size and micro-strain; b) Lattice parameters of Ti-doped ZnO nanostructures synthesized at different Ti content.

Fig. 2b shows the lattice parameters as a function of Ti content. As expected, the lattice parameters increase slightly with Ti content due to the fact that the ionic radius of Ti^{4+} is about 74.5 Å, whereas that of the Zn^{2+} is about 74 Å [64]. Similar behavior has been detected for the unit cell volume of the hexagonal structure of Ti-doped ZnO samples (Fig. 3a). To confirm the successful doping of ZnO with Ti, the interplanar d-spacing of different planes of Ti-doped ZnO nanostructures synthesized at different Ti content is calculated and shown in Fig. 3b.

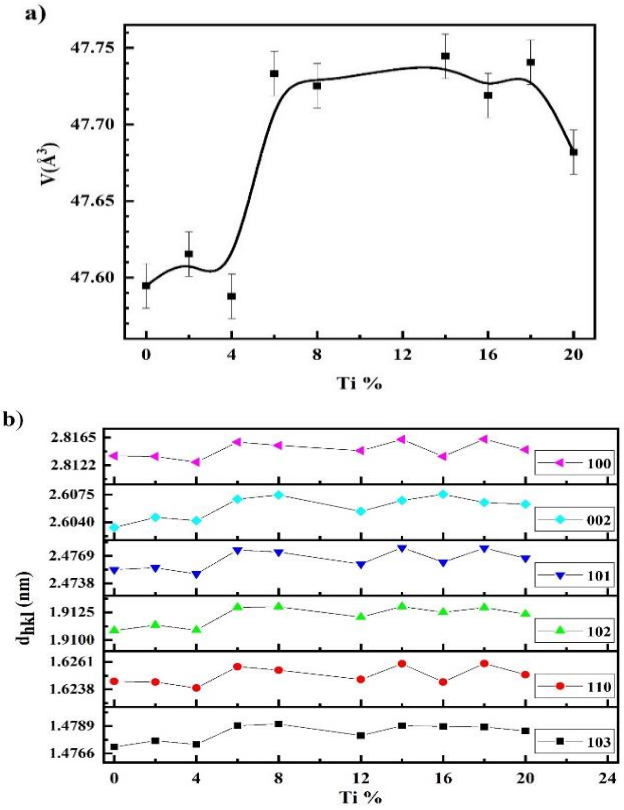

Fig. 3: a) Unit cell volume; (b) d-spacing of different planes of Ti-doped ZnO nanostructures synthesized at different Ti content.

It is evident that no significant change in the d-spacing values is detected for all Ti content. Similar observation is noted for Zn–O bond length calculated for undoped as well as Ti-doped samples, as enlisted in Table 2.

Table 2: Crystallite size and microstructural parameters obtained from the XRD analysis using Rietveld method.

Ti – content	Crystallite size (nm)	Micro-strain	Lattice parameters (Å)		Zn − O bond length ℓ (Å)	Unit cell volume V (Å^3)
			a	c		
0 %	44.3	0.004057	3.2489312	5.2066493	1.977436	47.59455
2 %	30.8	0.004706	3.2488317	5.209232	1.977706	47.61524
4 %	19.9	0.005234	3.247817	5.2083735	1.97718	47.57766
6 %	20.11	0.00504	3.2514105	5.213851	1.979334	47.73315
8 %	21.8	0.005485	3.2508147	5.2148943	1.979212	47.72521
12 %	23.4	0.004925	3.2452602	5.2047534	1.975682	47.46977
14 %	23.2	0.005253	3.2518897	5.2135525	1.979497	47.74449
16 %	18.11	0.004844	3.2488356	5.2150855	1.978412	47.66886
18 %	23.09	0.005569	3.2519338	5.2129827	1.979447	47.74057
20 %	17.28	0.005179	3.250057	5.2125783	1.978618	47.68178

Bearing in mind the very similar ionic radii of Zn^{2+} and Ti^{4+} ions, all these observations embody a clear indication that Ti is replacing the Zn atoms substitutionally (not interstitially) which confirms the successful doping. Our observations agree well with other reports in the literature [65].

Crystallite plot using anisotropic size-strain model (Popa rules model) for undoped as well as Ti-doped ZnO nanostructures synthesized at different Ti content is shown in Fig. 4. Obviously, crystallites are completely anisotropic, especially at low Ti concentration. This agrees well with the findings of the SEM study, as will be discussed in the next section.

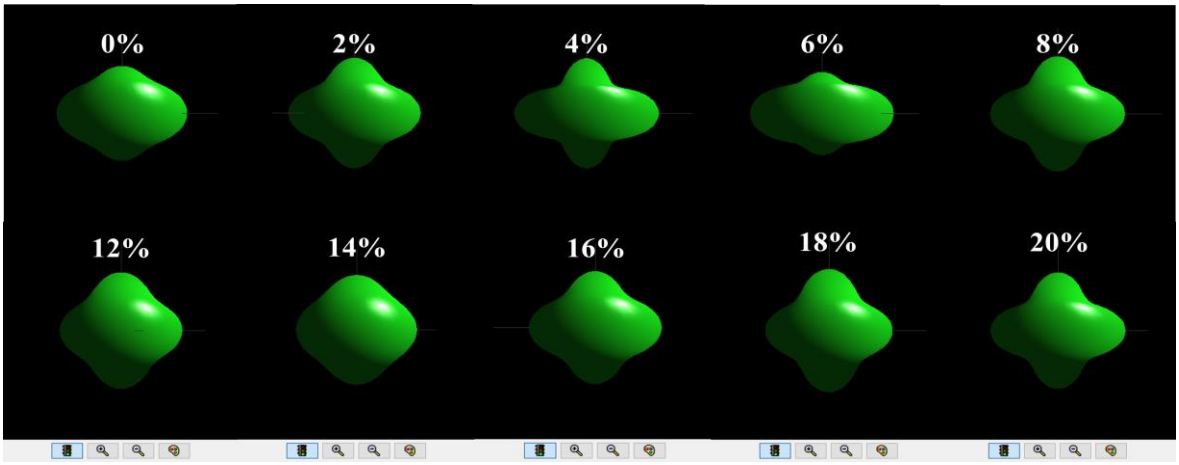

Fig. 4: Crystallite plot using Popa rules model for Ti-doped ZnO nanostructures synthesized at different Ti content.

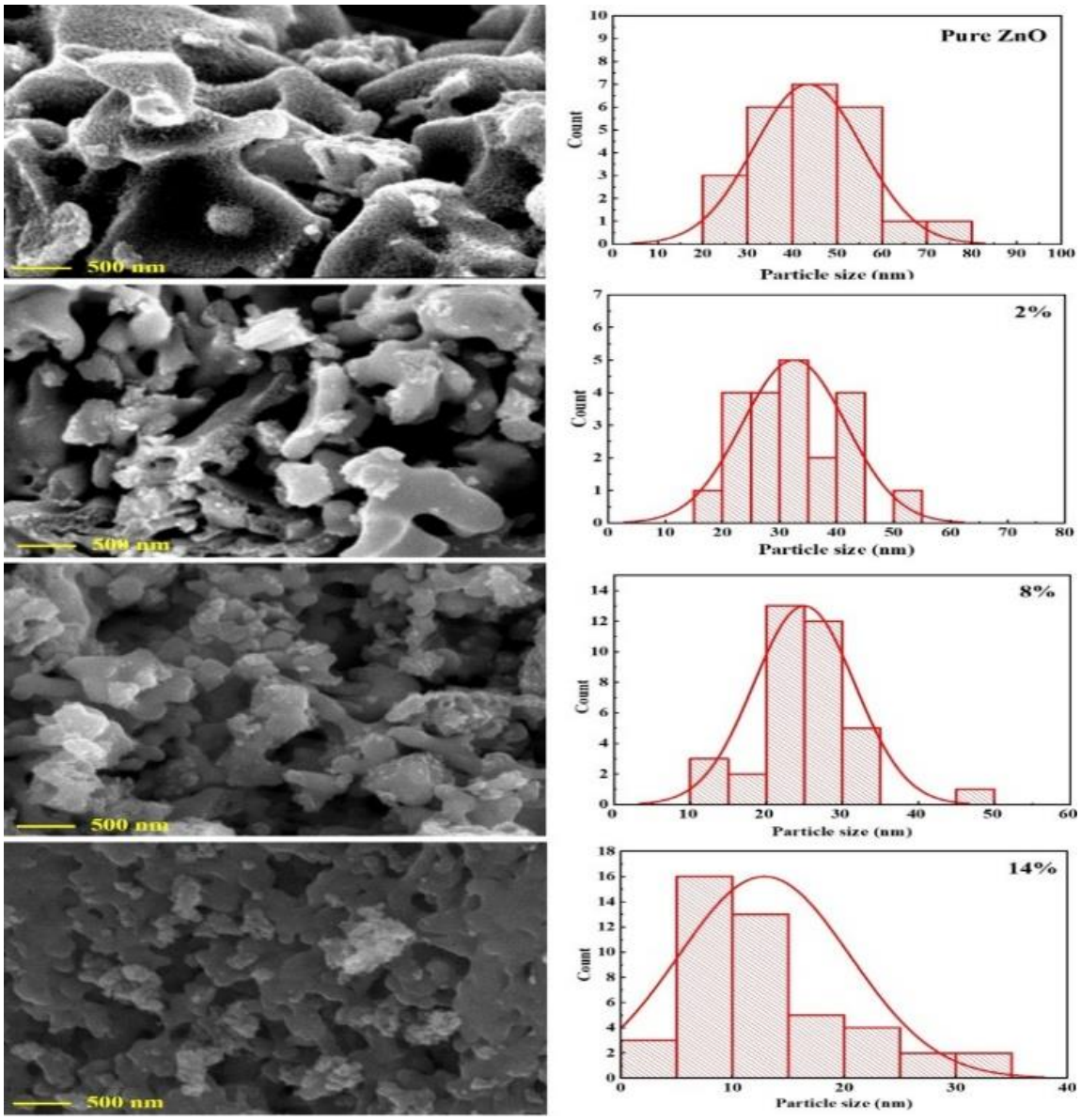

Fig. 5: SEM images and average size histograms of Ti-doped ZnO nanostructures synthesized at different Ti content.

3.2 SEM Measurements and EDX analysis

Fig. 5 shows SEM images and nanostructure size histograms of undoped as well as Ti-doped samples synthesized with different Ti content. It is evident that besides undoped ZnO samples, samples with 2% Ti-doping have nanoflakes morphology which has very important applications especially in sensors and dye-sensitized solar cells [66-68]. However, at higher content of Ti, doped samples show diverse morphology with porous nature which may be advantageous for photocatalytic reactions [4, 69, 70]. This could be due to the formation of nanoparticles with small size grown on the surface of the ZnO nanoflakes or due to spherical TiO_2 nanoparticles embedded in the ZnO matrix. The size distribution of the nanoflakes/nanostructures is estimated from the SEM images and analyzed using the ImageJ program [71]. The average size of the nanoflakes/nanostructures has been determined from the histogram and enlisted in table 3.

Clearly, as table 3 indicates, the average size of the nanoflakes/nanostructures estimated from the SEM images agrees will with the crystallite size estimated from the XRD measurements, except for high Ti-content where mixed oxide nanocomposites of ZnO – $ZnTiO_3$ are formed, which is expected due to the observed diverse morphology and porous nature of the samples, as previously discussed.

Table 3: The particle size is estimated by SEM Vs. the XRD calculated crystallite size.

Ti – content	Nanostructure average size estimated from SEM (nm)	Crystallite average size estimated from XRD (nm)
0 %	43.53	44.3
2 %	32.56	30.8
8 %	25.00	21.8
14 %	16.00	23.2

The elemental composition of undoped ZnO as well as Ti-doped ZnO samples synthesized with different Ti content is studied using EDX analysis. As shown in Fig. 6a, the only observed peaks in the EDX spectra of undoped ZnO samples are those of Zn and O at 0.98, 8.63, 9.55, and 0.52 keV, respectively. No impurities have been detected which ensures the purity of the samples. In the EDX spectra of Ti-doped samples (Fig. 6b-e), Ti peaks are detected at 4.5 keV and 4.95 keV. As shown, the intensity of the Ti peaks increases as the Ti/Zn molar ratio increases. This is further substantiated in table 4, which enlists the elemental composition of Ti-doped ZnO nanostructures synthesized at different Ti/Zn molar ratios. This again confirms the successful Ti-incorporation in the ZnO matrix.

Table 4: Elemental composition of Ti-doped ZnO nanostructures synthesized at different Ti/Zn molar ratios.

Ti/Zn molar ratio	Composition (at. %)		
	O	Zn	Ti
0	34.89±0.51	65.11±1.18	0
0.02	44.71±0.65	53.41±1.18	1.89±0.13
0.08	43.51±0.92	51.60±0.48	4.90±0.12
0.14	39.16±0.96	50.62±0.56	10.21±0.18
0.20	38.70±0.97	48.50±0.53	12.80±0.20

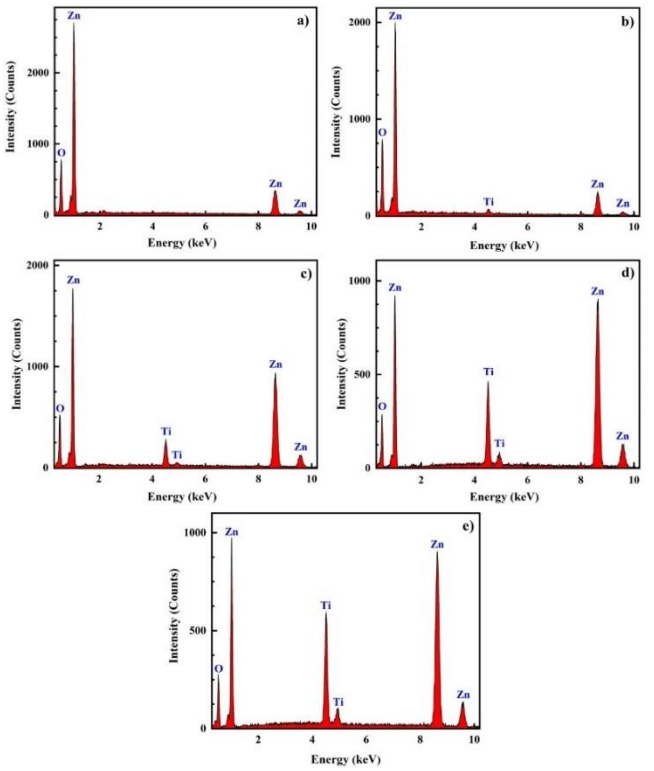

Fig. 6: EDX spectroscopy of Ti-doped ZnO nanostructures synthesized at different Ti/Zn molar ratios: a) 0, b) 0.02; c) 0.08; d) 0.14; e) 0.20

3.3 Optical Measurements

Fig. 7 shows the room temperature UV–V is absorption spectra of Ti-doped ZnO nanostructures synthesized at different Ti content. All samples show sharp absorption edge around 400 nm with a blue shift that is observed to increase with Ti doping. This absorption edge is clearly characteristic of ZnO. Another less prominent absorption edge around 320 nm (Inset of Fig. 7) is observed for doped samples with high Ti content ≥12%. This absorption edge is characteristic of the $ZnTiO_3$ phase [6, 59-61]. This corroborates our findings from the XRD analysis that at low Ti concentration, only Ti-doped ZnO nanostructures

are formed, while at high concentrations (≥12%) mixed oxide nanocomposites of ZnO – $ZnTiO_3$ are formed.

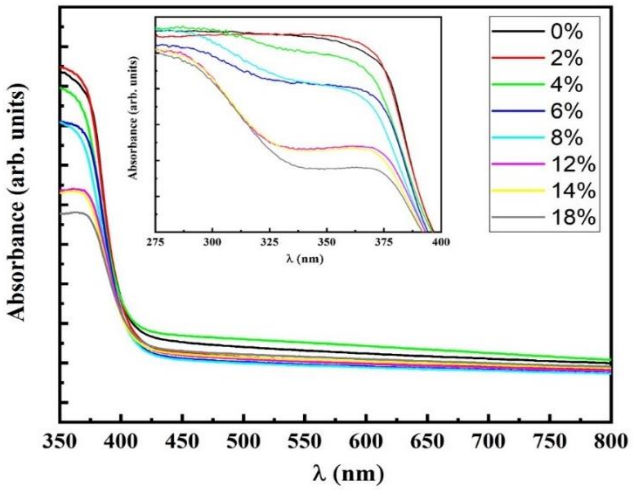

Fig. 7: Absorption spectra of Ti-doped ZnO nanostructures synthesized at different Ti content.

Fig. 8 shows UV–Vis diffuse reflectance spectra of Ti-doped ZnO nanostructures synthesized at different Ti content. Similar to the absorbance spectra, a blue shift is observed around 400 nm that increases with Ti doping. Furthermore, a second reflectance edge is formed around 320 nm for doped samples with high Ti content ≥12%.

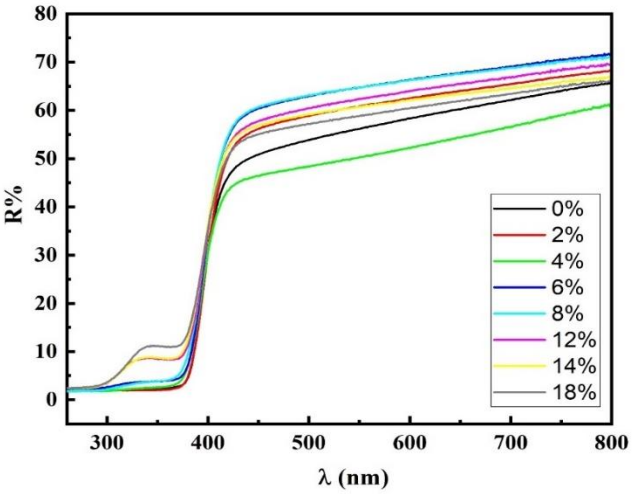

Fig. 8: Diffuse reflectance spectra of Ti-doped ZnO nanostructures synthesized at different Ti content.

In order to determine the bandgap of the synthesized samples using the diffuse reflectance spectra R, the Kubelka–Munk function $F_{KM}(R)$ is calculated using the formula [6, 58]:

$$F_{KM}(R) = \frac{(1-R)^2}{2R} \quad (12)$$

$F_{KM}(R)$ is proportional to the absorption coefficient α. The absorption coefficient α is related to the incident photon energy $h\nu$ as:

$$\alpha = \frac{K(h\nu - E_g)^{n/2}}{h\nu} \quad (13)$$

where K is a constant, E_g is the optical bandgap, and n is equal to 1 for direct bandgap material semiconductors. Since ZnO is a direct bandgap semiconductor material, the modified Kubelka–Munk function $(F_{KM}(R)\ h\nu)^2$ is plotted as a function of the energy $h\nu$ (in eV) as shown in Fig. 9.

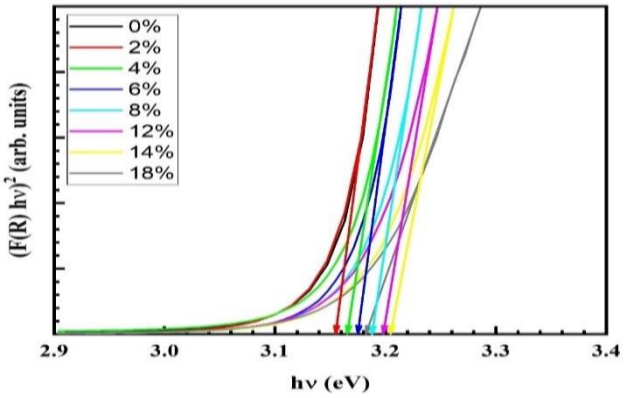

Fig. 9: Bandgap calculations of Ti-doped ZnO nanostructures synthesized at different Ti content.

By extrapolating the linear part to the energy axis, the value of the bandgap E_g is obtained for each sample. In agreement with the observed blue shift, the bandgap is found to increase with the Ti content as summarized in table 5.

Table 5: The bandgap of Ti-doped ZnO nanostructures synthesized at different Ti content.

Ti – content	Bandgap E_g (eV)
0 %	3.15
2 %	3.15
4 %	3.16
6 %	3.17
8 %	3.19
12 %	3.20
14 %	3.21

This result proves that the bandgap is sensitive to the Ti content and can be tuned by varying the Ti concentration. The obtained bandgap values agree well with previous results reported in the literature [4, 6, 59-61]. The observed bandgap increase with the increases of titanium concentration is attributed to the Burstein-Moss effect, where excessive carriers introduced by Ti doping fill the conduction band edge and leads to a displacement of the Fermi level which in turn widens the optical bandgap [59, 72-75].

4. Conclusions

The effect of Ti incorporation on the crystal structure, nanostructures size, shape, and elemental composition, as well as the optical properties of Ti-doped ZnO nanostructures is thoroughly studied using XRD, SEM, EDX, and UV-Vis Spectroscopy.

Mixed phases of hexagonal ZnO and cubic $ZnTiO_3$ are detected at high Ti concentrations (≥12%) and calcination temperatures of 600 °C. This is further confirmed by optical studies where absorbance as well as diffuse reflectance edges characteristic of $ZnTiO_3$ are detected. The crystallite size of the Ti-doped ZnO decreases (from 44.3 nm to 17.28 nm) as the Ti content increases in the ZnO host (from 0 % to 20 %). This is attributed to the presence of Ti^{4+} ions that decrease the number of reactive Zn^{2+} ions which, in turn, results in a slow nucleation process due to the lack of zinc citrate complex formation. Consequently, many defects/dislocations are introduced, and the micro-strain increases with increasing Ti content in the ZnO host.

The lattice parameters as well as the unit cell volume of the hexagonal structure of Ti-doped ZnO samples increase slightly with Ti content because the ionic radius of Ti^{4+} is about 74.5 Å, whereas that of the Zn^{2+} is about 74 Å. No significant change is observed in the calculated interplanar d-spacings or the Zn–O bond length of Ti-doped ZnO nanostructures synthesized at different Ti content, which provides a clear indication that Ti is replacing the Zn atoms substitutionally (not interstitially) and confirms the successful doping.

SEM studies show undoped ZnO as well as samples with 2% Ti-doping to have nanoflakes morphology, while at higher content of Ti, doped samples have diverse morphology with porous nature due to the formation of nanoparticles with small size grown on the surface of the ZnO nanoflakes or due to spherical TiO_2 nanoparticles embedded in the ZnO matrix. The intensity of the EDX Ti peaks detected at 4.5 keV and 4.95 keV and, accordingly the Ti-content, increases as the Ti/Zn molar ratio increases, which again confirms the successful Ti-incorporation in the ZnO matrix.

A blue shift is detected in the UV–Vis absorption and diffuse reflectance spectra of Ti-doped ZnO nanostructures synthesized at different Ti content. This shift is found to increase with Ti doping. Accordingly, the optical bandgap is found to be sensitive to the Ti content and can be tuned by varying the Ti concentration. The observed bandgap increase with the increases of titanium concentration is attributed to the Burstein-Moss effect.

References

[1] P. Rodnyi and I. Khodyuk, Optical and luminescence properties of zinc oxide (Review), Opt. Spectrosc . 111 (2011) 776-785.

[2] Ü. Özgür, Y. Alivov, C. Liu, A. Teke, M. Reshchikov, S. Doğan, V. Avrutin, S.-J. Cho, and H. Morkoç, A comprehensive review of ZnO materials and devices, J. Appl. Phys. 98 (2005) 11.

[3] R. Janisch, P. Gopal, and N. Spaldin, Transition metal-doped TiO_2 and ZnO – present status of the field, J. Phys. Condens. Matter. 17 (2005) R657-R689.

[4] R. Dhanalakshmi, A. Pandikumar, K. Sujatha, and P. Gunasekaran, Photocatalytic and antimicrobial activities of functionalized silicate sol–gel embedded ZnO–TiO_2 nanocomposite materials, Mater. Express 3 (2013) 291-300.

[5] L. Irimpan, B. Krishnan, V. Nampoori, and P. Radhakrishnan, Luminescence tuning and enhanced nonlinear optical properties of nanocomposites of ZnO – TiO_2, J. Colloid Interface Sci., 324 (2008) 99-104.

[6] M. Jose, M. Elakiya, and S. Dhas, Structural and optical properties of nanosized ZnO/$ZnTiO_3$ composite materials synthesized by a facile hydrothermal technique, J. Mater. Sci.: Mater. Electron. 28 (2017) 13649-13658.

[7] Y.-C. Lee, Y.-L. Huang, W.-H. Lee, and F.-S. Shieu, Formation and transformation of $ZnTiO_3$ prepared by sputtering process, Thin Solid Films 518 (2010) 7366-7371.

[8] J. Arin, S. Thongtem, and T. Thongtem, Single-step synthesis of ZnO/TiO_2 nanocomposites by microwave radiation and their photocatalytic activities, Mater. Lett. 96 (2013) 78-81.

[9] C. Klingshirn, ZnO: material, physics and applications, ChemPhysChem 8 (2007) 782-803.

[10] A. Moezzi, A. McDonagh, and M. Cortie, Zinc oxide particles: Synthesis, properties and applications, Chem. Eng. J. 185-186 (2012) 1-22.

[11] X. Chen and S. Mao, Titanium Dioxide Nanomaterials: Synthesis, Properties, Modifications, and Applications, Chem. Rev. 107 (2007) 2891-2959.

[12] S. Gupta and M. Tripathi, A review of TiO_2 nanoparticles, Chin. sci. bull. 56 (2011) 1639.

[13] D. Chen, H. Zhang, S. Hu, and J. Li, Preparation and Enhanced Photoelectrochemical Performance of Coupled Bicomponent ZnO − TiO2 Nanocomposites, J. Phys. Chem. C 112 (2008) 117-122.

[14] K. Klabunde and R. Richards, Nanoscale materials in chemistry, John Wiley & Sons, 2009.

[15] D. English, Book Review of Inorganic Nanoparticles: Synthesis, Applications, and Perspectives, J. Am. Chem. Soc. 133 (2011) 9626.

[16] K. Lu, Nanoparticulate materials: synthesis, characterization, and processing, John Wiley & Sons, 2012.

[17] F. Bensebaa, Nanoparticle Technology: from Lab to Market, ed: Elsevier Ltd., Amsterdam, 2012.

[18] S. Perween and A. Ranjan, Improved visible-light

photocatalytic activity in $ZnTiO_3$ nanopowder prepared by sol-electrospinning, Sol. Energy Mater. Sol. Cells 163 (2017) 148-156.

[19] H. Abe, J. Liu, and K. Ariga, Catalytic nanoarchitectonics for environmentally compatible energy generation, Mater. Today 19 (2016) 12-18.

[20] S. Stankic, S. Suman, F. Haque, and J. Vidic, Pure and multi metal oxide nanoparticles: synthesis, antibacterial and cytotoxic properties, J. Nanobiotechnology 14 (2016) 73.

[21] W. Park and K. Na, Advances in the synthesis and application of nanoparticles for drug delivery, Rev. Nanomed. Nanobiotechnol. 7 (2015) 494-508.

[22] J. Reinosa, P. Leret, C. Álvarez-Docio, A. del Campo, and J. Fernández, Enhancement of UV absorption behavior in ZnO – TiO_2 composites, Boletín de la Sociedad Española de Cerámica y Vidrio 55 (2016) 55-62.

[23] S. Ayed, R. Ben Belgacem, J. Zayani, and A. Matoussi, Structural and optical properties of ZnO/TiO_2 composites, Superlattices Microstruct. 91 (2016) 118-128.

[24] A. Mazabuel-Collazos, C. Gómez, and J. Rodríguez-Páez, ZnO – TiO_2 nanocomposites synthesized by wet-chemical route: Study of their structural and optical properties, Mater. Chem. Phys. 222 (2019) 230-245.

[25] S. Silva, F. Magalhães, and M. Sansiviero, Nanocompósitos semicondutores ZnO/TiO_2: testes fotocatalíticos, Quim. Nova 33 (2010) 85-89.

[26] G. Marcì, V. Augugliaro, M. López-Muñoz, C. Martín, L. Palmisano, V. Rives, M. Schiavello, R. Tilley, and A. Venezia, Preparation Characterization and Photocatalytic Activity of Polycrystalline ZnO/TiO2 Systems. 1. Surface and Bulk Characterization, J. Phys. Chem. B 105 (2001) 1026-1032.

[27] S. Liao, H. Donggen, D. Yu, Y. Su, and G. Yuan, Preparation and characterization of ZnO/TiO_2, $SO_4^{2-}/ZnO/TiO_2$ photocatalyst and their photocatalysis, J. Photochem. Photobiol. A: Chem. 168 (2004) 7-13.

[28] C. Cheng, A. Amini, C. Zhu, Z. Xu, H. Song, and N. Wang, Enhanced photocatalytic performance of TiO_2-ZnO hybrid nanostructures, Sci. Rep. 4 (2014) 4181.

[29] V. Lachom, P. Poolcharuansin, and P. Laokul, Preparation, characterizations and photocatalytic activity of a ZnO/TiO_2 nanocomposite, Mater. Res. Express 4 (2017) 035006.

[30] K. Shejale, D. Laishram, R. Gupta, and R. K. Sharma, Zinc Oxide – Titania Heterojunction-based Solid Nanospheres as Photoanodes for Electron-Trapping in Dye-Sensitized Solar Cells, Energy Technol. 5 (2017) 489-494.

[31] J. Chen, W. Liao, Y. Jiang, D. Yu, M. Zou, H. Zhu, M. Zhang, and M. Du, Facile Fabrication of ZnO/TiO_2 Heterogeneous Nanofibres and Their Photocatalytic Behaviour and Mechanism towards Rhodamine B, Nanomater. Nanotechnol. 6 (2016) 9.

[32] M. Konyar, D. Ovali, H. C. Yatmaz, C. Duran, and K. Öztürk, Photocatalytic efficiency of ZnO/TiO_2 composite plates in degradation of RR180 dye solutions, Adv. Sci. Technol. 65 (2010) 244-250.

[33] J. Guo, J. Li, A. Yin, K. Fan, and W. Dai, Photodegradation of Rhodamine B on Sulfur Doped ZnO/TiO_2 Nanocomposite Photocatalyst under Visible-light Irradiation, Chin. J. Chem. 28 (2010) 2144-2150.

[34] H. Bel Hadjltaief, M. Ben Zina, M. E. Galvez, and P. Da Costa, Photocatalytic degradation of methyl green dye in aqueous solution over natural clay-supported ZnO – TiO2 catalysts, J. Photochem. Photobiol. A: Chem. 315 (2016) 25-33.

[35] M. Gholami, M. Shirzad-Siboni, M. Farzadkia, and J.-K. Yang, Synthesis, characterization, and application of ZnO/TiO_2 nanocomposite for photocatalysis of a herbicide (Bentazon), Desalin. Water Treat. 57 (2016) 13632-13644.

[36] B. Yadav, R. Srivastava, and C. Dwivedi, Synthesis and characterization of ZnO – TiO_2 nanocomposite and its application as a humidity sensor, Philos. Mag. 88 (2008) 1113-1124.

[37] L. Gu, K. Zheng, Y. Zhou, J. Li, X. Mo, G. Patzke, and G. Chen, Humidity sensors based on ZnO/TiO_2 core/shell nanorod arrays with enhanced sensitivity, Sens. Actuators B Chem. 159 (2011) 1-7.

[38] N. Pandey, K. Tiwari, and A. Roy, ZnO – TiO_2 nanocomposite: Characterization and moisture sensing studies, Bull. Mater. Sci. 35 (2012) 347-352.

[39] K. Pan, Y. Dong, W. Zhou, Q. Pan, Y. Xie, T. Xie, G. Tian, and G. Wang, Facile Fabrication of Hierarchical TiO2 Nanobelt/ZnO Nanorod Heterogeneous Nanostructure: An Efficient Photoanode for Water Splitting, ACS Appl. Mater. Interfaces 5 (2013) 8314-8320.

[40] S. Hernández, V. Cauda, A. Chiodoni, S. Dallorto, A. Sacco, D. Hidalgo, E. Celasco, and C. Pirri, Optimization of 1D ZnO@TiO2 Core–Shell Nanostructures for Enhanced Photoelectrochemical Water Splitting under Solar Light Illumination, ACS Appl. Mater. Interfaces 6 (2014) 12153-12167.

[41] D. Barreca, E. Comini, A. P. Ferrucci, A. Gasparotto, C. Maccato, C. Maragno, G. Sberveglieri, and E.

Tondello, First example of ZnO − TiO2 nanocomposites by chemical vapor deposition: structure, morphology, composition, and gas sensing performances, Chem. Mater. 19 (2007) 5642-5649.

[42] Y. Dimitriev, Y. Ivanova, A. Staneva, L. Alexandrov, M. Mancheva, R. Yordanova, C. Dushkin , N. Kaneva , and C. Iliev, SYNTHESIS OF SUBMICRON POWDERS, J. Univ. Chem. Technol. Metall. 44 (2009) 235-242.

[43] A. Bachvarova-Nedelcheva, R. Iordanova, A. Stoyanova, R. Gegova, Y. Dimitriev, and A. Loukanov, Photocatalytic properties of ZnO/TiO_2 powders obtained via combustion gel method, Open Chem. 11 (2013) 364-370.

[44] K. Ohshima, K. Tsuto, K. Okuyama, and N. Tohge, Preparation of ZnO – TiO_2 Composite Fine Particles Using the Ultrasonic Spray Pyrolysis Method and Their Characteristics on Ultraviolet Cutoff, Aerosol Sci. Technol. 19 (1993) 468-477.

[45] X. Liu, Y.-y. Hu, R.-Y. Chen, Z. Chen, and H.-C. Han, Coaxial Nanofibers of ZnO – TiO_2 Heterojunction With High Photocatalytic Activity by Electrospinning Technique, Synth. React. Inorg. Met. Org. Chem. 44 (2014) 449-453.

[46] M. Habib, M. Shahadat, N. Bahadur, I. Ismail, and A. Mahmood, Synthesis and characterization of ZnO – TiO_2 nanocomposites and their application as photocatalysts, Int. Nano Lett. 3 (2013) 5.

[47] W. Ahmad, U. Mehmood, A. Al-Ahmed, F. Al-Sulaiman, M. Aslam, M. Kamal, and R. Shawabkeh, Synthesis of zinc oxide/titanium dioxide (ZnO/TiO_2) nanocomposites by wet incipient wetness impregnation method and preparation of ZnO/TiO_2 paste using poly(vinylpyrrolidone) for efficient dye-sensitized solar cells, Electrochim. Acta 222 (2016) 473-480.

[48] T. Suprabha, H. G. Roy, J. Thomas, K. P. Kumar, and S. Mathew, Microwave-assisted synthesis of titania nanocubes, nanospheres and nanorods for photocatalytic dye degradation, Nanoscale Res. Lett. 4 (2009) 144-152.

[49] R. Alwan, Q. Kadhim, K. Sahan, R. Ali, R. Mahdi, N. Kassim, A. Jassim, Synthesis of Zinc Oxide Nanoparticles via Sol – Gel Route and Their Characterization, Nanosci. Nanotech. 5 (2015) 1 – 6.

[50] S. Alias, A. Ismail, A. Mohamad, Effect of pH on ZnO nanoparticle properties synthesized by sol–gel centrifugation, J. Alloy Compd. 499 (2010) 231 – 237.

[51] M. Ciciliati, M. Silva, D. Fernandes, M. de Melo, A. Hechenleitner, E. Pineda, Fe-doped ZnO nanoparticles: Synthesis by a modified sol–gel method and characterization, Mater. Lett. 159 (2015) 84 – 86.

[52] A. Zak, M. Abrishami, W Abd. Majid, R. Yousefi, S. Hosseini, Effects of annealing temperature on some structural and optical properties of ZnO nanoparticles prepared by a modified sol–gel combustion method, Ceram. Int. 37 (2011) 393 – 398.

[53] K. Omri, I. Najeh, R. Dhahri, J. El Ghoul, L. El Mir, Effects of temperature on the optical and electrical properties of ZnO nanoparticles synthesized by sol–gel method, Microelectron. Eng. 128 (2014) 53 – 58.

[54] G. Williamson, W. Hall, X-ray line broadening from filed aluminium and wolfram, Acta Mettal. 1 (1953) 22 – 31.

[55] H. Rietveld, A Profile Refinement Method for Nuclear and Magnetic Structures, J. Appl. Cryst. 2 (1969) 65 – 71.

[56] N. Popa, The (*hkl*) Dependence of Diffraction-Line Broadening Caused by Strain and Size for all Laue Groups in Rietveld Refinement, J. Appl. Cryst. 31 (1998) 176 – 180.

[57] M. Abdel-Rahman, H. Ibrahim, Mostafa Y. A. Mostafa, M. A. Abdel-Rahman, M R Ebied and Emad A Badawi, The characterization of ZnO nanoparticles by applying x-ray diffraction and different methods of peak profile analysis, Phys. Scr. 96 (2021) 095704.

[58] R. López and R. Gómez, Band-gap energy estimation from diffuse reflectance measurements on sol – gel and commercial TiO_2: a comparative study, J. Solgel Sci. Technol. 61 (2012) 1-7.

[59] M. Yuste, R. Escobar-Galindo, N. Benito, C. Palacio, O. Martínez, J. Albella, and O. Sánchez, Effect of the Incorporation of Titanium on the Optical Properties of ZnO Thin Films: From Doping to Mixed Oxide Formation, Coatings 9 (2019) 180.

[60] R. Abirami, C. Kalaiselvi, L. Kungumadevi, T. Senthil, and M. Kang, Synthesis and characterization of $ZnTiO_3$ and Ag doped $ZnTiO_3$ perovskite nanoparticles and their enhanced photocatalytic and antibacterial activity, J. Solid State Chem. 281 (2020) 121019.

[61] L. Budigi, M. R. Nasina, K. Shaik, and S. Amaravadi, Structural and optical properties of zinc titanates synthesized by precipitation method, J. Chem. Sci. 127 (2015) 509 – 518.

[62] Y. Deng, Z. Zhou, Synthesis and crystal structure of a zinc citrate complex $[Zn(H_2cit)(H_2O)]_n$, J. Coord. Chem. 62 (2009) 1484 – 1491.

[63] I. Farbun, I. Romanova, T. Terikovskaya, D. Dzanashvili, S. Kirillov, Complex formation in the course of synthesis of zinc oxide from citrate

solutions, Russ. J. Appl. Chem. 80 (2007) 1798 – 1803.

[64] I. Darmadi, A. Taufik, and R. Saleh, Analysis of optical and structural properties of Ti-doped ZnO nanoparticles synthesized by co-precipitation method, J. Phys. Conf. Ser. 1442 (2020) 012021.

[65] M. Naeem, S. Qaseem, I. H. Gul, and A. Maqsood, Study of active surface defects in Ti doped ZnO nanoparticles, J. Appl. Phys. 107 (2010) 124303.

[66] S. Kanaparthi, and S. Singh, Chemiresistive sensor based on zinc oxide nanoflakes for CO_2 detection, ACS Appl. Nano Mater. 2 (2019) 700-706.

[67] Y. Kaneti, X. Zhang, M. Liu, D. Yu, Y. Yuan, L. Aldous, and X. Jiang, Experimental and theoretical studies of gold nanoparticle decorated zinc oxide nanoflakes with exposed {1 0 $\bar{1}$ 0} facets for butylamine sensing, Sens. Actuators B Chem. 230 (2016) 581-591.

[68] S. Al-Heniti, A. Umar, and H. M. Zaki, Synthesis and Characterization of Zinc Oxide Nanosheets for Dye-Sensitized Solar Cells, J. Nanosci. Nanotechnol. 15 (2015) 9954-9.

[69] M. H. Habibi and M. H. Rahmati, Fabrication and characterization of ZnO@CdS core-shell nanostructure using acetate precursors: XRD, FESEM, DRS, FTIR studies and effects of cadmium ion concentration on band gap, Spectrochim. Acta A. Mol. Biomol. Spectrosc. 133 (2014) 13-8.

[70] N. Hellen, H. Park, and K.-N. Kim, Characterization of ZnO/TiO_2 Nanocomposites Prepared via the Sol-Gel Method, J. Korean Ceram. Soc. 55 (2018) 140-144.

[71] https://imagej.nih.gov/ij/download.html

[72] Z. Ye, H. Lu, Y. Geng, Y. Gu, Z. Xie, Y. Zhang, Q. Sun, S. Ding, and D. Zhang, Structural, electrical, and optical properties of Ti-doped ZnO films fabricated by atomic layer deposition, Nanoscale Res. Lett. 8 (2013) 108.

[73] Synthesis of ZnO-TiO2 Nanoparticles by Sol-Gel Process and its Application for Solar Cell Semiconductor, Jurnal Kimia Valensi, Nanda Saridewi, Aditya Riyanti, Isalmi Aziz, Ade Lian Risa Adinda, Biaunik Niski Kumila Volume 10, No. 1, May 2024.

[74] Manganese doping on the structural properties of TiO2 and ZnO nanoparticles J. Phys.: Conf. Ser. 1442 012002, N F Djaja et al 2020.

[75] Effect of Mn doping on the structural and optical properties of sol-gel derived ZnO nanoparticles, Abdub G. Ali , Francis B. Dejene, Hendrik C. Swar**,** Cent. Eur. J. Phys. • 10(2) • 2012 • 478-484